



The Power of SOFIA/FORCAST in Estimating Internal Luminosities of Low-mass Class 0/I Protostars

Tracy L. Huard^{1,2}  and Susan Terebey³¹ Department of Astronomy, University of Maryland, College Park, MD 20742, USA² Columbia Astrophysics Laboratory, Columbia University, New York, NY 10027, USA³ Department of Physics and Astronomy, California State University at Los Angeles, Los Angeles, CA 90032, USA

Received 2017 July 7; revised 2017 November 8; accepted 2017 November 26; published 2017 December 19

Abstract

With the Stratospheric Observatory for Infrared Astronomy (SOFIA) routinely operating science flights, we demonstrate that observations with the Faint Object infraRed CAmera for the SOFIA Telescope (FORCAST) can provide reliable estimates of the internal luminosities, L_{int} , of protostars. We have developed a technique to estimate L_{int} using a pair of FORCAST filters: one “short-wavelength” filter centered within 19.7–25.3 μm , and one “long-wavelength” filter within 31.5–37.1 μm . These L_{int} estimates are reliable to within 30%–40% for 67% of protostars and to within a factor of 2.3–2.6 for 99% of protostars. The filter pair comprised of F 25.3 μm and F 37.1 μm achieves the best sensitivity and most constrained results. We evaluate several assumptions that could lead to systematic uncertainties. The OH5 dust opacity matches observational constraints for protostellar environments best, although not perfectly; we find that any improved dust model will have a small impact of 5%–10% on the L_{int} estimates. For protostellar envelopes, the TSC84 model yields masses that are twice those of the Ulrich model, but we conclude that this mass difference does not significantly impact results at the mid-infrared wavelengths probed by FORCAST. Thus, FORCAST is a powerful instrument for luminosity studies targeting newly discovered protostars or suspected protostars lacking detections longward of 24 μm . Furthermore, with its dynamic range and greater angular resolution, FORCAST may be used to characterize protostars that were either saturated or merged with other sources in previous surveys using the *Spitzer Space Telescope* or the *Herschel Space Observatory*.

Key words: dust, extinction – infrared: stars – radiative transfer – stars: formation – stars: luminosity function, mass function – stars: protostars

1. Introduction

The *Spitzer Space Telescope* enabled large infrared surveys of nearby star-forming molecular clouds, yielding a census of young stellar objects (YSOs) in each cloud. In particular, two *Spitzer* legacy projects, “From Molecular Cores to Planet-Forming Disks” (c2d; Evans et al. 2003) and “Gould’s Belt” (GB), observed star-forming regions in 18 molecular clouds, resulting in the identification of 2966 YSO candidates, including 326 protostellar (Class 0/I) candidates (Dunham et al. 2015). Two other *Spitzer* legacy projects were focused on the large star-forming regions of the Taurus (Rebull et al. 2010) and Orion (Megeath et al. 2012) molecular clouds, within which more than 3800 YSO candidates, including at least 500 protostellar candidates, were identified.

Since these *Spitzer* surveys, some studies using the *Herschel Space Observatory*—including the “Herschel Gould Belt Survey” (André et al. 2010)—have been published, identifying more protostars (e.g., Maury et al. 2011; Harvey et al. 2013; Stutz et al. 2013; Sadavoy et al. 2014). These additional protostars generally represent a small ($\lesssim 5\%$ – 10% ; e.g., Dunham et al. 2014) increase in the number of Class 0/I protostars identified with *Spitzer*, but they include “extreme Class 0” protostars, likely representing an earlier formation stage (Stutz et al. 2013; Dunham et al. 2014).

Among the most straightforward observational characteristics of protostars to derive is the bolometric luminosity, provided the spectral energy distributions (SEDs) are sufficiently covered, especially in the far-infrared and submillimeter regimes that dominate the emission. However, many protostars have not been observed at these wavelengths, and if they have, the observations may lack the angular resolution necessary to reliably characterize the thermal emission from dust in the protostellar envelope. Furthermore, the bolometric luminosity is “contaminated” by external heating by the interstellar radiation field; the *internal* (photospheric and accretion) luminosity, L_{int} , better represents an intrinsic property of the protostar. Differences between bolometric and internal luminosities tend not to be significant for typical or high-luminosity protostars; those with luminosities $\lesssim 1.0 L_{\odot}$ are most affected by external heating (e.g., Evans et al. 2001; Dunham et al. 2008; Whitney et al. 2013). Dunham et al. (2008) found that fluxes at 70 μm alone were reliable indicators of L_{int} .

Spitzer and *Herschel* surveys provided 70 μm fluxes for protostars, which may be used to estimate their internal luminosities. However, many protostars either lack 70 μm observations, or these observations suffer from insufficient dynamic range or angular resolution. With *Spitzer* and *Herschel* no longer obtaining such observations, a different approach is necessary to derive these estimates. We therefore use radiative transfer models to investigate, in a manner similar to that of Dunham et al. (2008), the relationships between internal luminosities and mid-infrared fluxes from the Faint Object infraRed CAmera for the SOFIA Telescope (FORCAST), which provides better dynamic range and angular



resolution. We demonstrate that FORCAST observations are sufficient to estimate internal luminosities of protostars with reliability comparable to that achieved by $70 \mu\text{m}$ observations. In Section 2 we summarize the protostar models used in this study. We discuss in Section 3 the relevant characteristics of FORCAST imaging observations adopted to survey these models. We present in Section 4 results from these models, which confirm consistency with previous studies; we characterize relationships between observed FORCAST fluxes and internal luminosities of protostars. In Section 5 we discuss the applicability and limitations of our results, and how these results may be used to further investigate low-mass protostars in nearby star-forming environments. We summarize our findings in Section 6.

2. Radiative Transfer Models

We employed the three-dimensional radiative transfer code HOCHUNK3D for protostars, which was developed by Whitney et al. (2013) based on the two-dimensional version (Whitney et al. 2003a, 2003b, 2004) that has been widely used in previous infrared surveys of protostars (e.g., Young et al. 2005; Haisch et al. 2006; Bolatto et al. 2007; Carlson et al. 2007, 2011; Chapman et al. 2007; Harvey et al. 2007; Hatchell et al. 2007; Simon et al. 2007; Tobin et al. 2007; Merín et al. 2008; Poulton et al. 2008; Seale & Looney 2008; Whitney et al. 2008; Enoch et al. 2009; Forbrich et al. 2010; Gramajo et al. 2010; Samal et al. 2012; Stutz et al. 2013). While HOCHUNK3D is equipped to deal with spiral and warp structures and gaps in the disk, our current study is focused on the two-dimensional structures of protostellar disks and envelopes.

Following Dunham et al. (2008), who used the RADMC code (Dullemond & Dominik 2004) to model protostars observed with *Spitzer* IRAC (3–8 μm ; Fazio et al. 2004) and MIPS (24, 70 μm ; Rieke et al. 2004), we considered 350 models of typical protostars and flared disks within rotationally flattened protostellar envelopes, heated by external interstellar radiation fields (ISRFs), with assumed properties as summarized in this section. For each model, we obtained results for 10 inclinations, i , uniformly spaced between $\cos i$ of 0 (edge-on disk) and 1 (face-on disk), or $\cos i = [0.05, 0.15, 0.25, \dots, 0.95]$; thus, 3500 SEDs were constructed with a distribution of inclinations reflecting that expected for real protostars randomly oriented. To limit statistical variations in the emergent fluxes, each model followed 10, 40, or 160 million photons, whichever was sufficient to yield signal-to-noise ratios (S/Ns) of at least 5 at all inclinations and wavebands considered in this study, where S/Ns were computed by HOCHUNK3D following Wood et al. (1996).

The protostars emit as blackbodies at temperature 3000 K with randomly selected (uniformly, in log space) luminosities in the range $0.03\text{--}30 L_{\odot}$, extending to more luminous protostars than Dunham et al. (2008). As mentioned in Crapsi et al. (2008), the precise temperature assumed for the protostars is not critical since all of the emission is reprocessed by the disks and envelopes.

The flared protostellar disks (e.g., Shakura & Sunyaev 1973; Pringle 1981; Lazareff et al. 1990; Bjorkman 1997; Hartmann 1998; Whitney et al. 2003b) have a density structure, ρ_{disk} , that decreases as a power law in the midplane radially (ϖ) while decreasing exponentially perpendicular to the

midplane (z) according to

$$\rho_{\text{disk}} = \rho_{d0} \left(1 - \sqrt{\frac{R_*}{\varpi}} \right) \left(\frac{R_*}{\varpi} \right)^{\beta+1} \exp \left\{ -\frac{1}{2} \left[\frac{z}{h(\varpi)} \right]^2 \right\}, \quad (1)$$

where R_* is the radius of the protostar, and the scale height increases as a power law, $h(\varpi) \propto (\varpi/R_*)^{\beta}$ with $\beta = 9/7$, which is consistent with a self-irradiated passive disk (Chiang & Goldreich 1997). No accretion energy is considered in the disks. The disks have inner radii given by the sublimation temperature and outer radii of 100 au, where the scale height is 20 au. The disk masses, which set the overall density normalizations, ρ_{d0} , are randomly selected (uniformly, in log space) in the range $10^{-5}\text{--}10^{-3} M_{\odot}$.

The rotationally flattened envelopes have density profiles, ρ_{env} , that may be parameterized in terms of the centrifugal radius, R_c , and the polar angle, θ_0 , of the streamline of infalling material at large radial distances, r (Ulrich 1976; Cassen & Moosman 1981):

$$\rho_{\text{env}} = \rho_o \left(\frac{R_c}{r} \right)^{3/2} \left(1 + \frac{\mu}{\mu_0} \right)^{-1/2} \left(\frac{\mu}{\mu_0} + \frac{2\mu_0^2 R_c}{r} \right)^{-1}, \quad (2)$$

where $\mu \equiv \cos \theta$ and $\mu_0 \equiv \cos \theta_0$. The constant ρ_o is defined by

$$\rho_o = \frac{\dot{M}_{\text{env}}}{4\pi \sqrt{G(M_* + M_{\text{disk}}) R_c^3}} \quad (3)$$

$$\approx \frac{\dot{M}_{\text{env}}}{4\pi \sqrt{GM_* R_c^3}}, \quad (4)$$

where \dot{M}_{env} is the mass infall rate in the envelope, M_* is the mass of the central protostar, M_{disk} is the mass of the disk, and $M_{\text{disk}} \ll M_*$. The Ulrich profile assumes that the gas is in free fall toward a fixed central mass. While the Ulrich profile is typically adopted for the entire envelope, as we have also done in our study, we remind readers that it most accurately reflects free-fall envelope densities at radial distances, r , within which the mass is dominated by the central protostar rather than the disk or envelope. Thus, the Ulrich profile deviates from an accurate collapse profile as the envelope mass interior to r increases appreciably relative to M_* (e.g., Shu 1977), which is likely the case in real protostellar envelopes (see Section 5).

In this formulation, the three input parameters \dot{M}_{env} , M_* , and R_c suffice to specify the envelope density profile. The parameters \dot{M}_{env} and M_* are related to the density normalization and collapse timescale. The parameter R_c is related to rotation and is often set equal to the disk radius. A fourth (less important) parameter arises because of the necessity to set a maximum cloud envelope radius, R_{env} , in order to compute a model. Other formulations of the Ulrich profile are present in the literature; for example, Furlan et al. (2016) preferred to express the profile in terms of the envelope density at a fiducial radial distance (1000 au), assuming $M_* = 0.5 M_{\odot}$. We instead have recast Equation (2) in terms of \dot{M}_{env} , which is often used in the literature, and use it to set the normalization instead of \dot{M}_{env} by noting that the streamlines become radial at large r , so that in the limit $r/R_c \rightarrow \infty$ and $\mu/\mu_0 \rightarrow 1$, the envelope

density simplifies to become

$$\rho_{\text{env}} \simeq \rho_o \left(\frac{R_c}{r} \right)^{3/2} 2^{-1/2}. \quad (5)$$

The mass of the envelope is then given by

$$M_{\text{env}} = 4\pi \int \rho_{\text{env}} r^2 dr \quad (6)$$

$$= \frac{2}{3} \frac{M_{\text{env}} R_{\text{env}}^{3/2}}{(2GM_*)^{1/2}}. \quad (7)$$

In order to facilitate comparison with the Dunham et al. (2008) and Crapsi et al. (2008) results, we adopt $M_* = 0.5 M_\odot$ for the model suite. Similarly, we consider envelopes with outer radii of 14,000 au, envelope masses randomly selected (uniformly, in log space) in the range 1–10 M_\odot , R_c randomly selected in the range 100–900 au, and bipolar cavities (created from protostellar outflows) with shape following the streamline with opening angle of 15° ; the density within each cavity is set to the density of the outermost region of the envelope (Dunham et al. 2008).

As discussed in Whitney et al. (2013), the external ISRF adopted by default in HOCHUNK3D is that found by Mathis et al. (1983) for the solar neighborhood, while Dunham et al. (2008) adopted that of Black (1994) modified at ultraviolet wavelengths for consistency with Draine (1978). Evans et al. (2001) discuss differences between these ISRFs, although we note that the default ISRF in HOCHUNK3D does not include the cosmic background component dominating at millimeter wavelengths. For consistency with Dunham et al. (2008), we adapted HOCHUNK3D to use the “Black-Draine” ISRF in our current study. To account for environmental differences among protostellar envelopes, including differing amounts of dust in the molecular clouds surrounding these envelopes, the strength of the ISRF was adjusted by a scale factor and then attenuated and reddened. For each envelope, this scale factor is randomly selected in the range 1/3–3, distributed logarithmically about unity, and the dust visual extinction is randomly selected in the range 1–5 magnitudes.

2.1. Dust Grain Properties

The optical properties of the envelope dust adopted by Dunham et al. (2008) were not available; therefore, we experimented with different dust grain populations available in the literature. The first three grain populations that we considered were readily available in the HOCHUNK3D distribution. The first population, which we refer to as “KMH-ice” dust, was that found by Kim et al. (1994) for the average Galactic interstellar medium, except with water-ice mantles making up the outer 5% (in radius) of the grains. The second population that we tried was the “molecular cloud model” (hereafter, referred to as “MCM”) dust appropriate for protostellar envelopes and described in Whitney et al. (2013). The third dust population was “model 1” dust, which we refer to as “WM1” dust, used by Wood et al. (2002) to model the disk of the classical T Tauri star HH 30 IRS. A fourth population was the thinly ice-mantled, coagulated dust of Ossenkopf & Henning (1994), often referred to as “OH5” grains in the literature (e.g., Evans et al. 2001; Shirley et al. 2005), augmented by the opacities of Pollack et al. (1994) at wavelengths shorter than $1.25 \mu\text{m}$, as described in

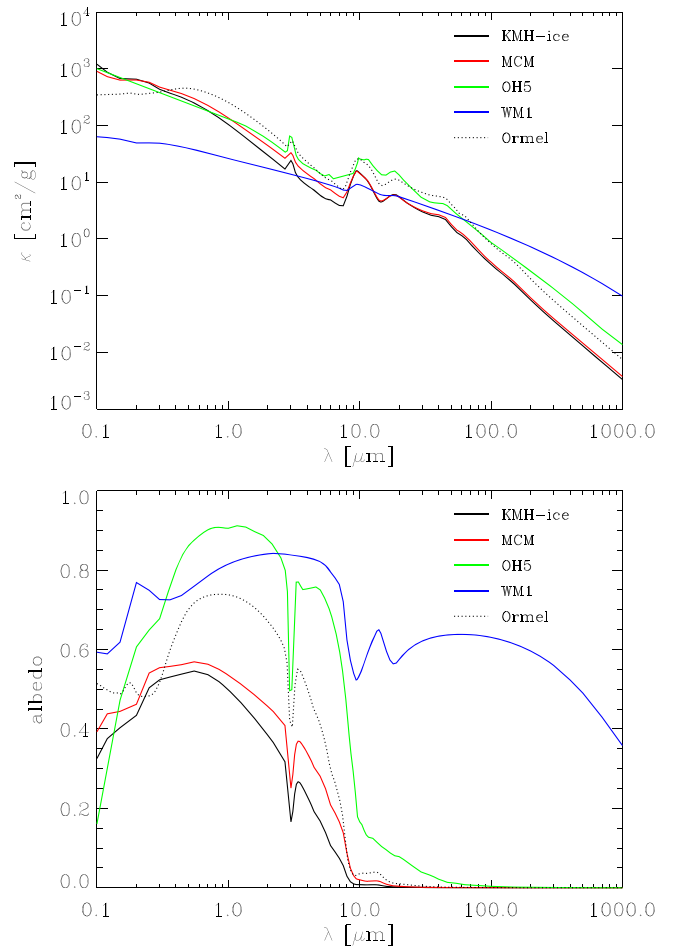


Figure 1. Opacities (top) and albedos (bottom) of the gas and dust mixture, assuming a gas-to-dust mass ratio of 100, for the different grain populations considered in this study.

Dunham et al. (2010). The last population was that of Ormel et al. (2011) adopted by Furlan et al. (2016), which includes a mixture of ice-coated silicate and bare graphite grains of radii $0.1\text{--}3 \mu\text{m}$. The OH5 and Ormel populations were not available in HOCHUNK3D, but we included them for this study. For reference, the opacities and albedos for the five considered grain populations are shown in Figure 1.

Observationally derived, infrared and submillimeter dust opacities for protostellar environments relative to the opacity at $2.2 \mu\text{m}$ are shown in Figure 2. A comparison with the relative opacities from grain populations considered in this study suggests that the OH5 grains best reproduce these observations. For this reason, we adopt the OH5 population in this study.

As evident in Figure 2, none of the grain populations yield relative opacities at $1.2\text{--}850 \mu\text{m}$ that are fully consistent with observations. Increasing the relative opacity of OH5 grains by 35% for $\lambda \geq 2.5 \mu\text{m}$ yields better agreement with observations. In order to obtain some handle on how a grain population better constructed for protostellar environments may affect our results, we reran the models with these “revised OH5” opacities. We stress, however, that artificially increasing the mid-infrared and submillimeter relative opacities of the OH5 grains is not consistent with element abundance constraints of grain populations; such opacities would result from larger grains, and inclusion of these larger grains would necessarily come at the expense of smaller grains to conserve element

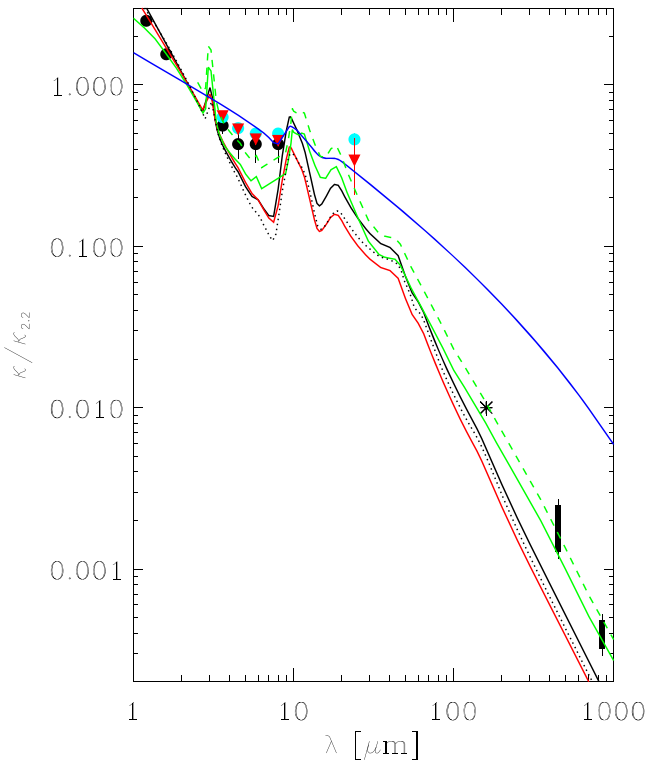


Figure 2. Comparison of observationally derived dust opacities relative to that at $2.2 \mu\text{m}$ in protostellar environments and dense molecular clouds with those of grain populations considered in this study. Observed relative opacities at $1.2\text{--}24 \mu\text{m}$ from Indebetouw et al. (2005), Flaherty et al. (2007), and Chapman et al. (2009) are plotted as filled black circles, light blue circles, and red triangles; the 160 and $250 \mu\text{m}$ relative opacities from Terebey et al. (2009) and Suutarinen et al. (2013) are plotted as an asterisk and open circle, respectively; and the relative opacity ranges at 450 and $850 \mu\text{m}$ from Shirley et al. (2011) are plotted as vertical bars. Error bars have been included, although in most cases, they are covered by the symbol. The relative opacities of grain populations are plotted as curves with the same color scheme as in Figure 1: KMH-ice (black), MCM (red), WM1 (blue), OH5 (green), and Ormel (black dotted curve). The dashed green line represents the relative opacity of the OH5 population, increased by 35% for $\lambda \geq 2.5 \mu\text{m}$.

abundances. Constructing a protostellar grain population is beyond the scope of this study.

3. FORCAST Filters and Sensitivities

The FORCAST instrument (Adams et al. 2010; Herter et al. 2012) on the Stratospheric Observatory for Infrared Astronomy (SOFIA; Young et al. 2012) obtains mid-infrared images and spectra at $5.4\text{--}37.1 \mu\text{m}$ on two detectors: the short-wavelength channel (SWC), and the long-wavelength channel (LWC). Using a dichroic, these channels simultaneously image two wavebands; alternatively, a single channel may be used to directly image one waveband. For our study, we consider only FORCAST images using the seven filters, listed in Table 1, in the range $19.7\text{--}37.1 \mu\text{m}$ for typical observing conditions: specifically, an altitude of 41,000 feet, $7.1 \mu\text{m}$ of precipitable water vapor at the zenith, and telescope pointings at 50° from the zenith (e.g., Horn & Becklin 2001).

For purposes of discussion, we adopt fiducial sensitivity limits as those point-source flux densities associated with $S/N = 3$ after an hour exposure time. Most FORCAST surveys of star-forming regions are likely to require greater S/N s achieved in reasonable times; thus, we expect that most

Table 1
Fiducial Sensitivity Limits

FORCAST Filter ^a	Dichroic (mJy)	Direct (mJy)
F 19.7 μm (SWC)	25	23
F 24.2 μm (LWC)	...	50
F 25.3 μm (SWC)	63	59
F 31.5 μm (LWC)	84	60
F 33.6 μm (LWC)	182	116
F 34.8 μm (LWC)	114	78
F 37.1 μm (LWC)	168	97

Note.

^a For each filter, the channel is included in parentheses.

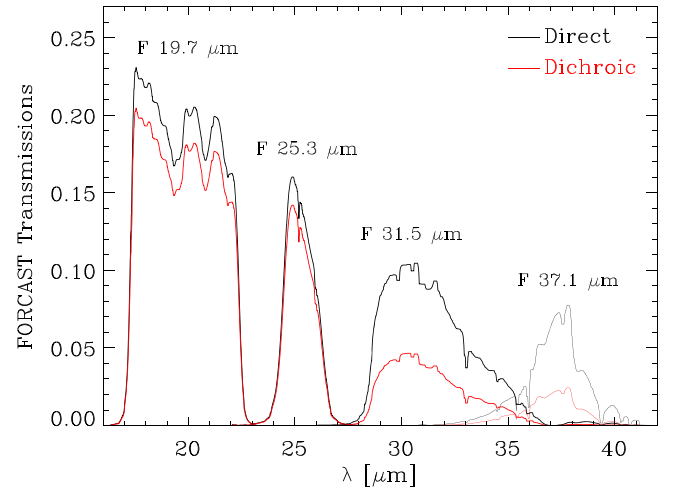


Figure 3. Effective transmission functions of four of the seven FORCAST filters considered in this study, assuming typical observing conditions. The functions associated with observations obtained in direct and dichroic modes are plotted as black and red curves, respectively, and account for absorption by the atmosphere and optical elements as well as the detector response.

studies will focus on sources brighter than given by these limits. Using the online SOFIA Instrument Time Estimator⁴, we determined these fiducial sensitivity limits, in typical observing conditions, for the FORCAST filters operating in direct and dichroic modes, as listed in Table 1.

Figure 3 illustrates the effective transmissions of four of these FORCAST filters, accounting for the atmosphere, optics (e.g., the filter itself, optical blockers, and dichroic, as appropriate), and detector response. Except for the F 24.2 μm filter, which operates only in direct mode, we included in HOCHUNK3D the dichroic transmission functions of the filters listed in Table 1 in order to derive FORCAST flux densities of protostellar models. For the F 24.2 μm filter, we included the direct transmission function. For each filter, the shapes of the direct and dichroic transmission functions are similar; the primary difference is in the overall scale factor of the transmission. Therefore, no significant difference is expected in flux densities derived from dichroic and direct transmission functions, only in the observing time required to detect them, particularly for filters with effective wavelengths greater than $30 \mu\text{m}$.

⁴ <https://dcs.sofia.usra.edu/proposalDevelopment/SITE/>

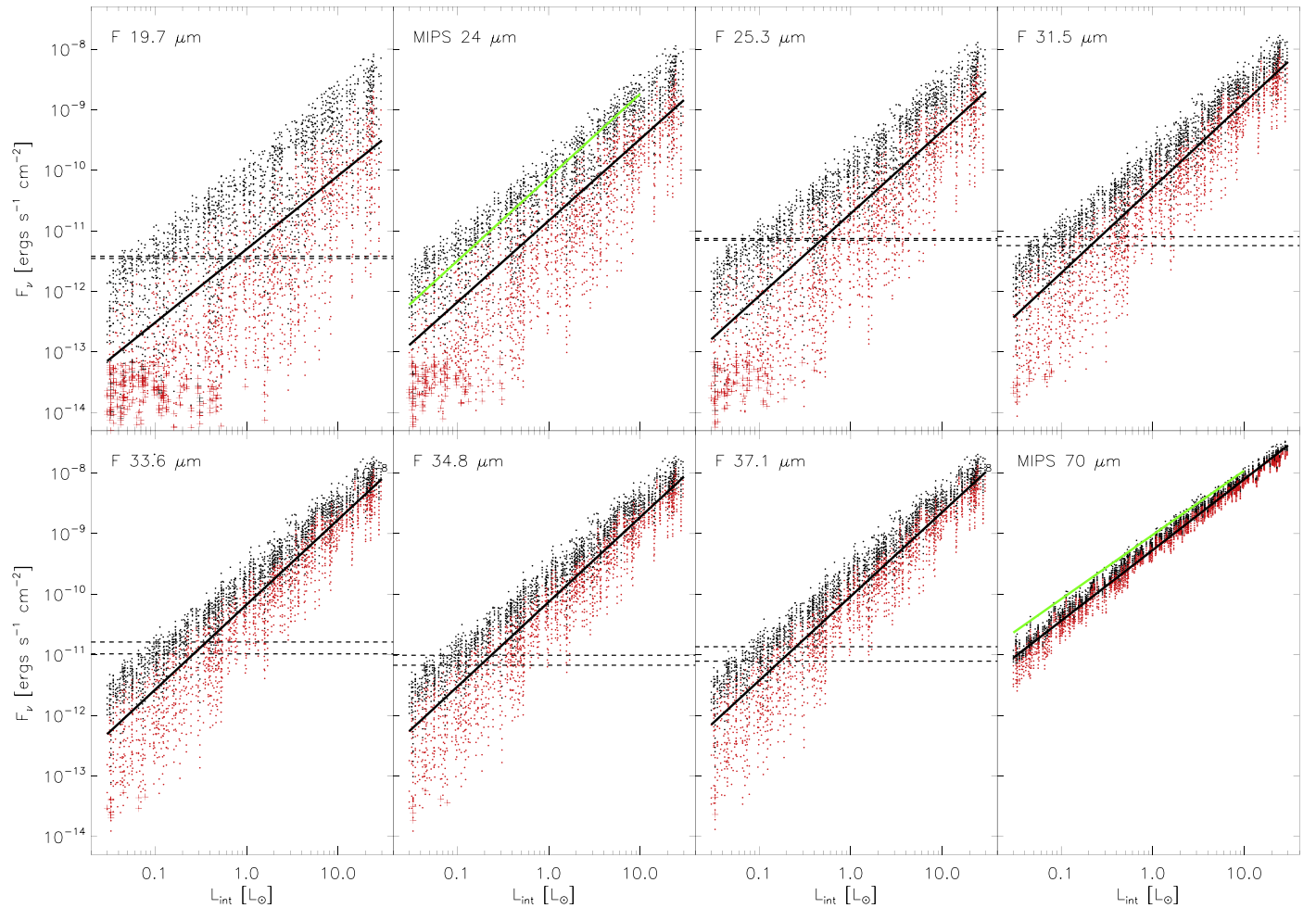


Figure 4. MIPS and FORCAST fluxes as a function of L_{int} for protostellar disks and envelopes with OH5 dust. Each FORCAST panel also includes horizontal dashed lines representing the fiducial sensitivity limits for that filter in dichroic (top dashed line) and direct (bottom dashed line) modes, as listed in Table 1. The black and red points represent our models with $\cos i \geq 0.5$ and $\cos i < 0.5$, respectively. The models that are dominated by photons originating from the ISRF (see Section 5) are identified by plus signs; FORCAST is not sensitive to such models. Our best-fit lines to all models, excluding the ISRF-dominated models, are shown as black lines. The MIPS 24 and 70 μm panels include the fits from Dunham et al. (2008) as green lines for reference.

4. Results

Following the approach of Dunham et al. (2008) and adopting OH5 dust, as discussed in Section 2.1, our results for FORCAST and MIPS fluxes at a distance of 140 pc and as a function of L_{int} are shown in Figure 4, demonstrating that L_{int} is best indicated by the 70 μm flux. This figure illustrates increased scatter, particularly at smaller wavelengths and for lower luminosity protostars. The increased scatter is primarily due to geometric effects of inclination. Scatter introduced from inclination may be understood by referring to the SEDs of a standard Class I protostar shown in Figure 14 of Whitney et al. (2013). The flux at 70 μm is relatively unchanged with inclination, while fluxes at shorter wavelengths, particularly for $\lambda < 40 \mu\text{m}$, vary considerably for the same protostar observed at different inclinations.

Like Dunham et al. (2008), we derive fluxes within 6'' radius (840 au at 140 pc) apertures, which is the *Spitzer* resolution (FWHM) at 24 μm , for $\lambda < 40 \mu\text{m}$ and within 20'' radius (2800 au at 140 pc) apertures at 70 μm . Typical resolutions achieved by FORCAST filters in 19.7–37.1 μm are 2''1–3''4; thus, in principle, our aperture fluxes for FORCAST filters will capture a greater fraction of the total fluxes. At least for point sources, the 6'' radius aperture already captured most of the flux

in *Spitzer* observations; any difference between 6'' radius aperture fluxes derived from *Spitzer* observations and those derived from FORCAST observations is expected to be negligible.

Using a linear least-squares fitting method, we determined the best-fit parameter values, m and b , characterizing the dependence of flux, F_ν (measured in $\text{erg s}^{-1} \text{cm}^{-2}$) at a distance 140 pc, on L_{int} (measured in L_\odot):

$$\log F_\nu = m \log L_{\text{int}} + b, \quad (8)$$

where we note that observed photometry is typically given in terms of flux density, $S_\nu = F_\nu \nu^{-1}$. The best fits are illustrated in Figure 4, and the associated parameter values are listed in Table 2, which also lists the standard reduced chi-squared χ_{red}^2 statistics for assessing the quality of these fits. More directly meaningful is Column 5 of Table 2, which lists values for the dispersion (σ) between best-fit and input $\log L_{\text{int}}$ values

$$\sigma_L \equiv \sigma [\log L_{\text{int}}(\text{fit}) - \log L_{\text{int}}], \quad (9)$$

where the best-fit values can be explicitly written, for clarity, as

$$\log L_{\text{int}}(\text{fit}) = \frac{\log F_\nu - b}{m}, \quad (10)$$

Table 2
Single-filter Fits

Filter	m	b	χ_{red}^2	σ_L^a
MIPS 24 μm	1.35 ± 0.02	-10.83 ± 0.01	298	0.56
MIPS 70 μm	1.169 ± 0.003	-9.270 ± 0.002	10	0.12
F 19.7 μm	1.21 ± 0.02	-11.30 ± 0.02	477	0.55
F 24.2 μm	1.36 ± 0.01	-10.68 ± 0.01	256	0.39
F 25.3 μm	1.36 ± 0.02	-10.71 ± 0.01	278	0.38
F 31.5 μm	1.41 ± 0.01	-10.289 ± 0.009	143	0.29
F 33.6 μm	1.40 ± 0.01	-10.173 ± 0.008	121	0.26
F 34.8 μm	1.400 ± 0.009	-10.129 ± 0.008	112	0.25
F 37.1 μm	1.391 ± 0.009	-10.035 ± 0.007	97	0.24

Note.

^a σ_L represents the dispersion between best-fit and input $\log L_{\text{int}}$ values. For MIPS filters, all models are considered; for FORCAST filters, only models detectable given the fiducial sensitivities in dichroic mode (except for F 24.2 μm , where we assumed direct mode) are considered.

using the values for m and b listed in Table 2. These dispersions, σ_L , provide a direct means for quantifying the reliability of L_{int} estimates based on these fits. For example, $\sigma_L = 0.12$ when using 70 μm fluxes; thus, L_{int} estimates based on these fluxes are reliable to within a factor of 1.3 for 67% of the models (i.e., 1σ) and 2.3 for 99% of the models (i.e., 3σ), assuming normal distributions. In contrast, the 19.7 μm fluxes, which yield $\sigma_L = 0.55$, result in luminosities reliable only to within a factor of 45 (3σ ; factor of 3.5 for 1σ). Clearly, the capability that *Spitzer* and *Herschel* had in obtaining 70 μm fluxes was critical in characterizing protostars.

Equation (10), with fluxes at an adopted distance of 140 pc, may be converted into a form directly applicable to observations, for which S_ν is typically given in Jy and valid for any distance d , as

$$L_{\text{int}}(\text{fit}) = \left[\left(\frac{d}{140 \text{ pc}} \right)^2 \frac{\nu S_\nu}{10^{23+b}} \right]^{1/m} L_\odot, \quad (11)$$

where ν is the effective frequency, given in Hz, of the filter, and the best-fit parameter values m and b may be obtained from Table 2. Focusing on 70 μm , for example, L_{int} may be estimated using

$$L_{\text{int}}(\text{fit}) = 0.115 \left[\left(\frac{d}{140 \text{ pc}} \right)^2 S_{\nu,70} \right]^{0.855} L_\odot. \quad (12)$$

Thus, a protostar observed at 70 μm to be 1 Jy at a distance of 140 pc suggests that L_{int} is $\sim 0.1 L_\odot$, reliable to within a factor of 2.3 (3σ), as previously discussed.

With the scatter in the correlations between FORCAST fluxes and L_{int} being primarily a function of inclination, we explored whether using two FORCAST fluxes may improve estimates of L_{int} . Again referring to Figure 14 of Whitney et al. (2013), the slopes of the SEDs in the 20–40 μm regime appear to be correlated with inclination, suggesting that two FORCAST fluxes would in principle provide a first-order luminosity estimate from the average flux level and second-order correction to the estimate from the slope. For example, Kryukova et al. (2012) found that for protostars lacking 70 μm fluxes, better luminosity estimates could be achieved by

considering both the *Spitzer* 24 μm fluxes and slopes of available 3.6–24 μm SEDs than by considering the 24 μm fluxes alone. Such luminosity estimates were reliable to within a factor of ~ 11 (3σ), compared to a factor of 48 (3σ ; from $\sigma_L = 0.56$ in Table 2) based on 24 μm fluxes alone, representing a marked improvement.

Our approach to use two FORCAST fluxes is similar to that by Kryukova et al. (2012) to use *Spitzer* 3.6–24 μm SEDs, but we might expect a greater improvement since FORCAST extends to longer mid-infrared wavelengths. Toward this end, we considered pairs of FORCAST filters, where the first filter was one of longer wavelengths (i.e., 31.5–37.1 μm) and the second filter was one of shorter wavelengths (i.e., 19.7–25.3 μm). Linear regression was then used to determine the best-fit coefficients to

$$\log L_{\text{int}} = C_1 \log F_{\nu_1} + C_2 \log F_{\nu_2} + C_3, \quad (13)$$

where the fluxes at 140 pc associated with Filter 1 and Filter 2 are denoted as F_{ν_1} and F_{ν_2} , respectively. Table 3 lists these coefficients for the different filter pairs, and Figure 5 compares $L_{\text{int}}(\text{fit})$ with those input into the model. In general, there is reasonable agreement for all models, particularly those detectable by FORCAST, with increased dispersion for intrinsically fainter protostars. Similar to Table 2, Table 3 also lists values for σ_L to quantify the reliability of luminosity estimates based on these fits for all models detectable by FORCAST.

Regardless of the FORCAST filter combination, the two-filter fits provide luminosity estimates that are reliable at least to within a factor of 2.6 (3σ). Filter combinations including F 25.3 μm generally provide the most constrained estimates. The best FORCAST filter combination is F 37.1 μm with F 25.3 μm , which yields $\sigma_L = 0.12$, providing luminosities reliable to within a factor of 2.3 (3σ), comparable to that achieved from 70 μm observations.

Our fits to Equation (13) may be recast in a form more directly applicable to observations of a source at distance d , in general, as

$$L_{\text{int}}(\text{fit}) = \Lambda \left(\frac{d}{140 \text{ pc}} \right)^{2(C_1+C_2)} S_{\nu_1}^{C_1} S_{\nu_2}^{C_2} L_\odot, \quad (14)$$

where S_{ν_1} and S_{ν_2} are the observed flux densities in Jy in Filters 1 and 2, respectively, and Λ is the coefficient accounting for the conversion of units and overall normalization given by

$$\Lambda = \frac{\nu_1^{C_1} \nu_2^{C_2}}{10^{23(C_1+C_2)-C_3}}, \quad (15)$$

where ν_1 and ν_2 are the effective frequencies, in Hz, associated with Filters 1 and 2, respectively. For example, focusing explicitly on 37.1 μm and 25.3 μm , L_{int} may be estimated using

$$L_{\text{int}}(\text{fit}) = 0.226 \left(\frac{d}{140 \text{ pc}} \right)^{1.444} (S_{\nu,37.1})^{1.409} \times (S_{\nu,25.3})^{-0.687} L_\odot, \quad (16)$$

where the flux densities $S_{\nu,37.1}$ and $S_{\nu,25.3}$ are given in Jy.

While FORCAST filter pairs yield L_{int} estimates with a reliability comparable to the reliability achieved previously with 70 μm observations, observational biases are evident in Figure 5 and depend on the specific filter pair, protostellar

Table 3
Two-filter Fits

Filter 1	Filter 2	C_1	C_2	C_3	σ_L^a
F 37.1 μm	F 19.7 μm	1.032 ± 0.005	-0.322 ± 0.004	6.671	0.13
F 37.1 μm	F 24.2 μm	1.484 ± 0.009	-0.763 ± 0.009	6.716	0.13
F 37.1 μm	F 25.3 μm	1.409 ± 0.009	-0.687 ± 0.008	6.754	0.12
F 34.8 μm	F 19.7 μm	1.058 ± 0.006	-0.361 ± 0.005	6.590	0.13
F 34.8 μm	F 24.2 μm	1.62 ± 0.01	-0.91 ± 0.01	6.63	0.13
F 34.8 μm	F 25.3 μm	1.52 ± 0.01	-0.815 ± 0.009	6.681	0.13
F 33.6 μm	F 19.7 μm	1.074 ± 0.006	-0.384 ± 0.005	6.532	0.14
F 33.6 μm	F 24.2 μm	1.71 ± 0.01	-1.01 ± 0.01	6.56	0.13
F 33.6 μm	F 25.3 μm	1.60 ± 0.01	-0.90 ± 0.01	6.62	0.13
F 31.5 μm	F 19.7 μm	1.131 ± 0.007	-0.455 ± 0.006	6.443	0.14
F 31.5 μm	F 24.2 μm	2.04 ± 0.02	-1.35 ± 0.01	6.48	0.14
F 31.5 μm	F 25.3 μm	1.86 ± 0.01	-1.17 ± 0.01	6.56	0.13

Note.

^a σ_L represents the dispersion between best-fit and input $\log L_{\text{int}}$ values for models detected with FORCAST in both filters.

luminosity, and sensitivity of the FORCAST observations. Brighter protostars are preferentially detected, resulting in fitted luminosity estimates that systematically overestimate L_{int} , which is especially evident for low-luminosity protostars $L_{\text{int}} < 0.3 L_{\odot}$ observed with a filter pair that includes F 19.7 μm . The filter combination F 37.1 μm with F 25.3 μm shows the least bias, although the luminosities are still overestimated for the lowest luminosity protostars. The degree to which L_{int} estimates are biased increases for relatively low-luminosity protostars and for less sensitive observations.

Figure 5 also shows that nearly all FORCAST-detectable models lie within the $3\sigma_L$ ranges, extrapolated from computed σ_L dispersions listed in Table 3, suggesting that these ranges overestimate the ranges associated with 99% of FORCAST-detectable models. For example, a careful analysis that accounts for the asymmetric and non-normal distribution suggests that $L_{\text{int}}(\text{fit})$ is consistent with L_{int} to within a factor of 1.9–2.1 for 99% of models detectable by F 37.1 μm and F 25.3 μm , slightly smaller than the factor of 2.3 extrapolated from σ_L . (A difference in σ_L of only 0.01–0.02 accounts for this effect.) In other words, σ_L slightly *understates* the reliability of L_{int} estimates derived from FORCAST filter pairs. Given different systematic uncertainties, such as discussed in Sections 5.2 and 5.3, we continue to adopt σ_L from Table 3 as they are conservative measures of the reliability of L_{int} estimates.

5. Discussion

As illustrated in Figures 4 and 5, FORCAST is not sensitive to the faintest of protostars. While protostars at 140 pc with $L_{\text{int}} \gtrsim 0.2 L_{\odot}$ are detectable at 37.1 μm , only those more luminous than $\sim 0.7 L_{\odot}$ are detectable at 19.7 μm . Our method to use a pair of FORCAST filters to determine internal luminosities of protostars is viable for protostars detectable in these filters, which is driven primarily by the sensitivity at shorter wavelengths. Thus, the choice of filter pair is important. Furthermore, the viability of this method is not solely a function of the internal luminosity, but inclination and other properties play a role as well.

In Figure 6 we explore the interplay of internal luminosity, envelope mass, and inclination in determining the detectability of protostars with two different filter pairs: F 37.1 μm with

F 19.7 μm ; and F 37.1 μm with F 25.3 μm . Comparing the two left panels, we see that protostars of lower luminosities are detectable when using F 25.3 μm rather than F 19.7 μm , as expected, especially for greater envelope masses. While envelope mass affects detectability, it has less impact (i.e., the solid and dotted curves exhibit steeper slopes) when using F 25.3 μm . Comparing each of the right panels with its adjacent left panel, we see that a greater fraction of lower luminosity protostars are detectable when models with nearly edge-on protostars are excluded.

The sensitivity of F 25.3 μm , over that of F 19.7 μm , to more models is a compelling reason to favor it. As previously mentioned, Table 3 demonstrates that F 25.3 μm paired with F 37.1 μm yields L_{int} estimates with less uncertainty. Given these considerations of completeness and precision, observations of protostars with F 37.1 μm and F 25.3 μm are likely best for the purpose of determining L_{int} .

We find models for which more than half of the radiation within 20'' radius (2800 au at 140 pc) apertures are reprocessed or scattered photons originating from the external ISRF rather than from the protostellar system. While such observed ISRF photons are dependent on the strength of field, extinction from the parental molecular cloud, and properties of the protostellar envelope, they are not tied to the internal protostellar luminosity. Thus, contribution (or ‘‘contamination’’) from the ISRF primarily serves to add scatter in the relationships between F_{ν} and L_{int} , and it enables a guide to the level of precision possible on estimates of L_{int} for protostellar systems in a typical range of environments. ISRF-dominated models are more prevalent at 19.7 μm than at 25.3 μm and are found more for nearly edge-on, less luminous protostars. While HOCHUNK3D enables tracking of the sources of the photons imaged from each system, an observer, in general, does not know a priori the relative contribution of the ISRF. It may be possible to estimate this contamination based on the observed radial profile, enabling results with better L_{int} precision. For our study, we did not pursue such an investigation since we were able to estimate L_{int} with precision comparable to that provided by *Spitzer* and *Herschel*. Furthermore, models dominated by the ISRF in the mid-infrared FORCAST bands are at least two orders of magnitude below the fiducial FORCAST sensitivity limits.

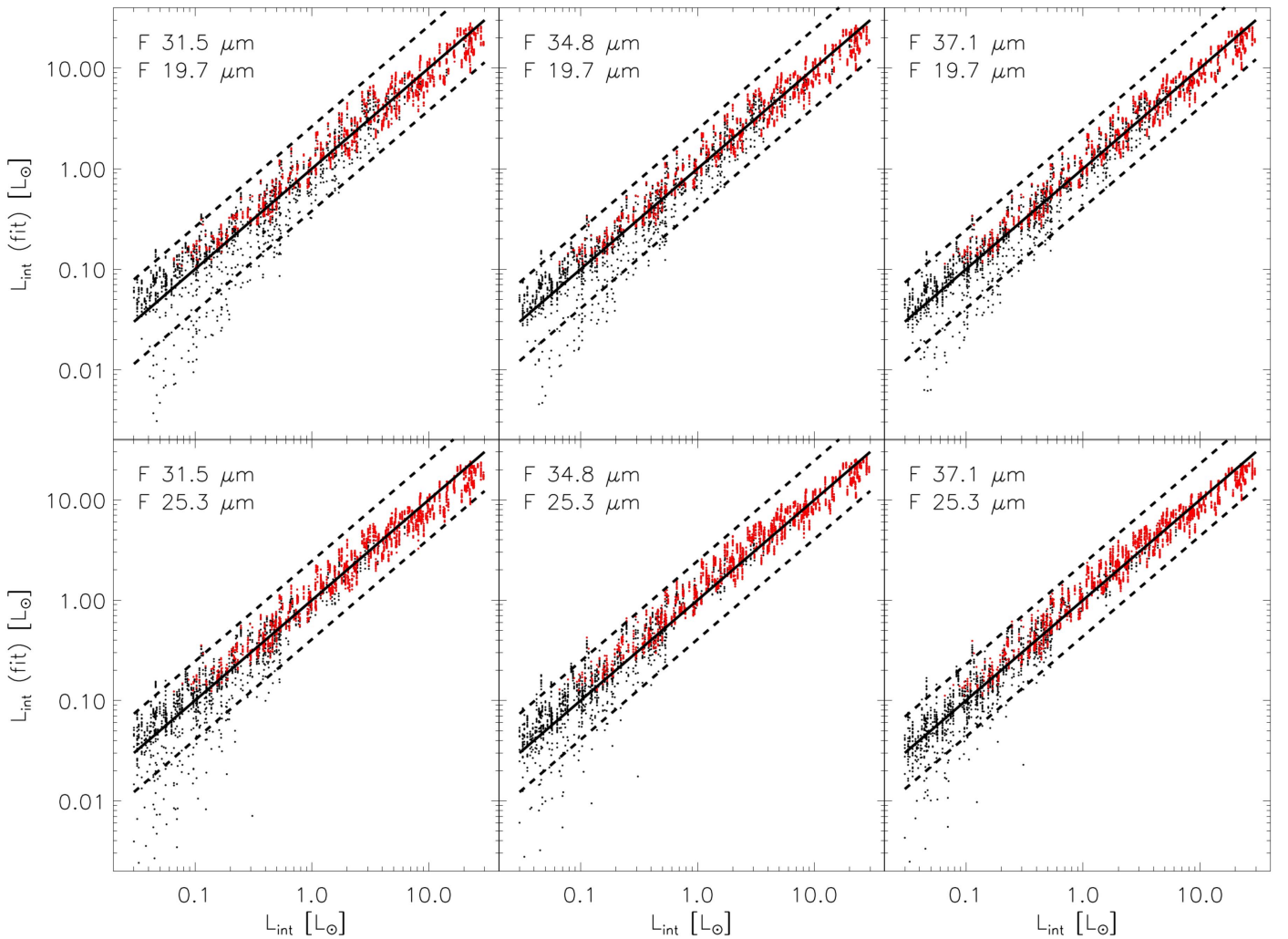


Figure 5. Comparison of L_{int} estimates, derived from mid-infrared fluxes, with input L_{int} for half of the two-filter combinations considered in this study. Plots associated with L_{int} estimates using long-wavelength filters F 31.5 μm , F 34.8 μm , and F 37.1 μm are plotted in the left, center, and right panels; estimates using short-wavelength filters F 19.7 μm and F 25.3 μm are plotted in the top and bottom panels. These plots are similar to those using filters F 24.2 μm and F 33.6 μm , which are not included in this figure. The black points represent models with a flux in at least one of the two relevant FORCAST bands less than the dichroic fiducial sensitivity limit; the red points represent models detectable within the fiducial 1 hr exposures. ISRF-dominated models are not included. The solid lines represent perfect agreement between the estimates and model input values, while the dashed lines represent estimates within $3\sigma_L$ ranges.

5.1. Inclination and External Heating

Traditionally, the luminosity of a protostar has been determined by integrating an SED, which requires sufficient spectral coverage, especially from the infrared to submillimeter regimes. We refer to this luminosity as the *observed* bolometric luminosity, $L_{\text{bol}}(\text{SED})$. The evacuated cavity and protostellar disk primarily, and envelope density profile secondarily, result in a non-uniform escape of infrared photons. Light detected from a pole-on protostar suffers less extinction relative to the same protostar observed edge-on. Therefore, $L_{\text{bol}}(\text{SED})$ will overestimate the *true* bolometric luminosity in the case of the pole-on protostar and underestimate it for the edge-on protostar. This effect, which we refer to as the “flashlight effect,” has been documented in the literature (e.g., Yorke & Bodenheimer 1999; Whitney et al. 2003b; Zhang et al. 2013). For example, in their Figure 10, Whitney et al. (2003b) demonstrated that $L_{\text{bol}}(\text{SED})$ overestimated the true bolometric luminosity by about a factor of 2 for their pole-on protostars with bipolar cavities and underestimated it by 50% for the same protostars observed edge-on. Our models show a similar trend.

The bolometric luminosity includes the internal luminosity of the protostar as well as a component, or “contamination,” due to external heating by the ISRF. For our models, this contamination is typically $\sim 0.3 L_{\odot}$, consistent with previous studies (e.g., Evans et al. 2001), and reaches as high as $\sim 1 L_{\odot}$ in some cases. Thus, not only does $L_{\text{bol}}(\text{SED})$ suffer from the flashlight effect, but the contamination from external heating can be significant, particularly for protostars with $L_{\text{int}} \lesssim 1 L_{\odot}$.

In our method for estimating protostellar luminosities from FORCAST fluxes, the fluxes were empirically fit to L_{int} according to Equation (13); thus, it calibrates out the effect of external heating, in a statistical sense. But does our method suffer from the flashlight effect? Using a pair of FORCAST filters was intended to account for inclination, the primary factor in the large scatter in correlations between FORCAST fluxes and L_{int} shown in Figure 4. In Figure 7 we plot L_{int} relative to $L_{\text{int}}(\text{fit})$ derived from F 37.1 μm and F 25.3 μm as a function of inclination, demonstrating that our method results in reliable luminosity estimates that do not depend on inclination. Plots for other filter pairs show similar results. Thus, our method successfully uses pairs of FORCAST filters

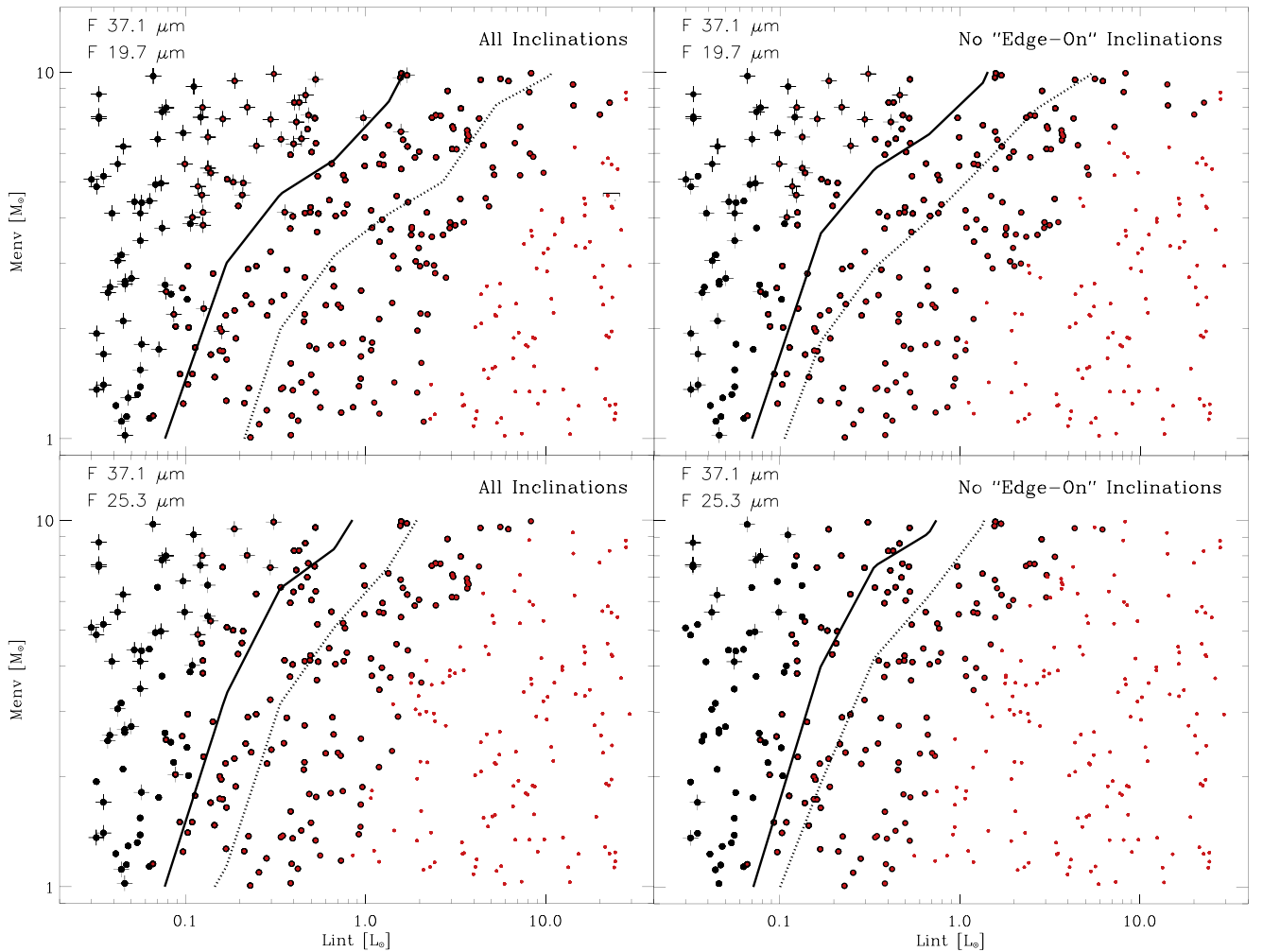


Figure 6. Comparison of $(L_{\text{int}}, M_{\text{env}})$ parameter space probed by our models and those detectable by FORCAST, for select pairs of filters and inclinations. Top panels show models observed with filters F 37.1 μm and F 19.7 μm ; bottom panels show models observed with filters F 37.1 μm and F 25.3 μm . Left panels include models for all inclinations, while the right panels exclude models with nearly edge-on inclinations (specifically, with $\cos i < 0.2$). First, models that are undetectable by FORCAST are plotted with larger and thicker black symbols, and then models that are detectable by FORCAST are overplotted as smaller and thinner red symbols. The symbol is a dot for a model dominated by protostellar radiation; it is a plus sign for a model dominated by scattered or reprocessed radiation from the ISRF. Note that there are no red plus signs plotted since all models dominated by ISRF are undetectable by FORCAST and therefore appear as black plus signs. Since there are 10 models (one for each inclination) for each $(L_{\text{int}}, M_{\text{env}})$ probed, only red dots appear for the models that are detectable for all inclinations; red dots on top of larger black dots appear for models detectable for only some inclinations; and only larger black dots appear for models undetectable for all inclinations. Finally, the dotted and solid curves correspond to the region where 50% and 25%, respectively, of the models are detectable by FORCAST.

to estimate L_{int} to better characterize protostars more efficiently than obtaining a full SED to determine $L_{\text{bol}}(\text{SED})$.

5.2. Consideration of Aperture Sizes

Deriving FORCAST fluxes from 6'' radius apertures enabled us to compare our results directly with Dunham et al. (2008), who used the same aperture size for 10–40 μm . In principle, the flux-luminosity relationships derived by our study and by Dunham et al. (2008) apply strictly to fluxes derived with the same physical size of the aperture—i.e., a radius of 840 au. In practice, however, because these apertures include most (typically $\gtrsim 90\%$) of the mid-infrared emission from the protostars, it is not important to adhere to the same physical aperture size when deriving fluxes for protostars at different distances if the apertures include a larger physical area. For example, one could simply use 6'' radius apertures to measure fluxes for all protostars in the GB molecular clouds, with distances ~ 140 –500 pc. The relatively small amount of flux

added by including a region of 3000 au for protostars at 500 pc compared to a region of 840 au for those at 140 pc potentially introduces a systematic error that is insignificant compared to other dominant systematic errors. Furthermore, since our relationships involve pairs of FORCAST filters, such a systematic error is expected to be even more muted since the measured mid-infrared FORCAST fluxes will be increased similarly in both filters when increasing the physical aperture size.

We tested these expectations explicitly by using total flux densities (obtained from large 100'' radius apertures capturing emission from the entire protostellar envelope of outer radius 14,000 au) in the relationships given by Equation (14) to derive L_{int} estimates that were typically within 5% of those obtained from the 6'' radius apertures from which the relationships were derived. We do not recommend using Equations (14) or (16) with flux densities obtained from apertures much smaller than 840 au since the more extended size of the protostar (from scattered light) at shorter FORCAST wavelengths relative to

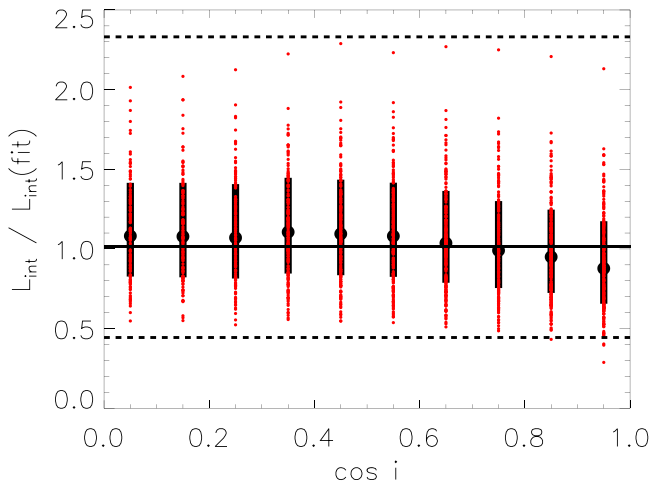


Figure 7. Plot of $L_{\text{int}}/L_{\text{int}}(\text{fit})$ as a function of $\cos i$ for models detectable by FORCAST filters F 37.1 μm and F 25.3 μm , demonstrating that our method using this filter pair yields L_{int} estimates that do not depend on inclination. Individual models are represented by red points (the same models plotted by red points in the bottom right panel of Figure 5), while the median and dispersion (computed in log space) at each inclination are represented by the black filled circles and error bars. The horizontal solid line represents the median value for all detectable models, and dashed lines represent the $3\sigma_L$ range. Plots for other filter pairs show similar results.

that at longer wavelengths may result in greater systematic errors.

5.3. Impact of Dust Grain Population

While OH5 grain opacities are most consistent with observational constraints, there are discrepancies, as discussed in Section 2.1. To quantify the impact of the shortcoming of OH5 grains on L_{int} estimates derived from a pair of FORCAST filters, we reran our protostellar models using “revised OH5” grains, with 35% greater opacity for $\lambda \geq 2.5 \mu\text{m}$ compared to OH5 grains. The flux densities at 37.1 μm and 25.3 μm for all FORCAST-detectable models were used to obtain L_{int} estimates using Equation (16). These estimates were typically $\sim 5\%$ lower than those obtained using OH5 grains; most models with revised OH5 grains yielded L_{int} estimates that were within 5%–10% of those obtained with OH5 grains. We therefore expect any improved dust model to have a relatively small effect on our results.

5.4. Applicability of Our Results

We stress that our results apply to embedded protostellar sources at an early evolutionary stage exhibiting a protostellar envelope, as described in Section 2. Historically, such protostars have been observationally identified as Class 0 or Class I (hereafter, Class 0/I) sources, based on thermal dust emission or the slopes, α , of the infrared SEDs (Lada 1987; Andre et al. 1993). Class 0/I sources are commonly defined as those with $\alpha \geq 0.3$, while Flat sources are those with $0.3 > \alpha \geq -0.3$ and Class II sources, primarily representing evolved YSOs, are those with $-0.3 > \alpha \geq -1.6$ (Greene et al. 1994).

While sources observationally identified as Class 0/I are likely bona fide protostars with envelopes, it is possible that some of these sources instead are the more evolved Class II sources obscured by sufficient molecular cloud

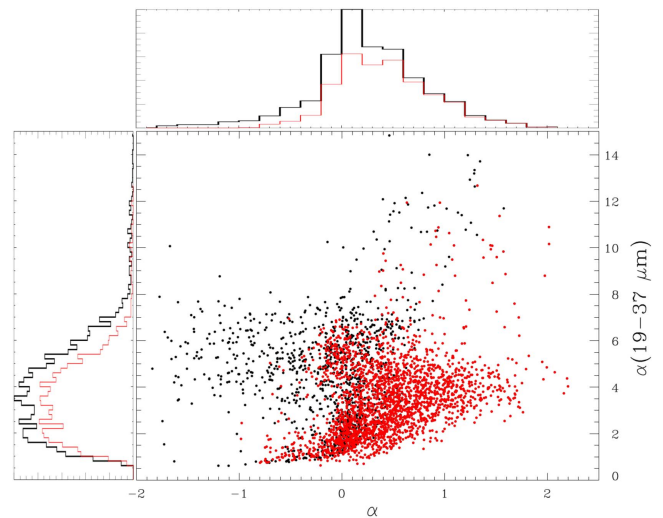


Figure 8. Slopes of the SEDs characteristic of our protostellar models. The mid-infrared slopes α (19–37 μm), derived from FORCAST bands, are plotted relative to the infrared slopes α traditionally defined by the 2–24 μm bands. Models detectable by FORCAST are plotted as red points, while models not detectable are plotted as black points. The histograms along the left represent the distributions of α (19–37 μm), with black showing the distribution for all models and red showing that for only the detectable models. The histograms along the top represent the distributions of α , with the same color scheme. Focusing on the FORCAST-detectable models, the median slopes are $\alpha \sim 0.3$ and $\alpha(19\text{--}37 \mu\text{m}) \sim 3.5$, with 95% of these models falling into the following ranges: $\alpha = [-0.3, 0.2]$ and $\alpha(19\text{--}37 \mu\text{m}) = [1, 6.5]$.

material such that their SEDs mimic those of protostars. Such “contamination” is most prevalent in embedded young clusters, where the intracluster material may provide significant extinction along the lines of sight. Based on a *Spitzer* study of the NGC 2264 and IC 348 clusters (Forbrich et al. 2010), up to a third of sources previously identified as Class 0/I were found to be consistent with extinguished Class II sources, although half of these possibly extinguished Class II sources are also still consistent with being Class 0/I protostars. More recently, Carney et al. (2016) use $\text{HCO}^+ J = 3\text{--}2$, $\text{C}^{18}\text{O} J = 3\text{--}2$, and 850 μm observations to distinguish Class 0/I protostars from extinguished Class II sources in Perseus and Taurus; they found that $\sim 30\%$ of sources classified as Class 0/I based on their SEDs were likely extinguished Class II sources. Thus, most sources classified as Class 0/I based on their infrared SEDs are bona fide Class 0/I protostars, especially in relatively isolated star-forming regions, with no more than $\sim 20\%$ – 30% expected to be extinguished Class II sources in regions of embedded clusters. If a source exhibits $\alpha \geq 0.3$, it is most likely a protostar, and our results most likely apply.

A source exhibiting $\alpha < 0.3$ may also be a protostar described by our modeling; in fact, the distribution of α exhibited by our models, shown in Figure 8, peaks at $\alpha \sim 0.1$ and shows an extended tail for $\alpha \leq -0.3$, slopes that are more indicative of flat-spectrum and Class II sources. Since most decreasing infrared SEDs are associated with Class II sources, additional evidence beyond the 2–24 μm SED would be necessary to believe reasonably that a particular source with such an SED is a protostar, rather than an evolved Class II source.

The case for identifying a source as a protostar may be bolstered by FORCAST 19–37 μm observations. Figure 8 shows that *all* protostellar models exhibit mid-infrared SED slopes, $\alpha(19\text{--}37 \mu\text{m}) > 0.5$, in the FORCAST bands. Our

distribution of $\alpha(19\text{--}37\ \mu\text{m})$ is consistent with previously published SEDs. For example, inspection of the SEDs of a standard Class I protostar from Whitney et al. (2013; Figure 14) suggests that $\alpha(19\text{--}37\ \mu\text{m}) \gtrsim 1$ for all inclinations; earlier stage Class 0 protostars would exhibit greater values. Furthermore, inspection of the SEDs of Class II sources from Whitney et al. (2013; Figure 2) suggests flatter mid-infrared SED slopes, with $\alpha(19\text{--}37\ \mu\text{m}) \lesssim 0.5$ for most inclinations; only relatively edge-on inclinations with $\cos i \lesssim 0.25$ have $\alpha(19\text{--}37\ \mu\text{m})$ that rival those of protostars.

The identification and classification of protostars is beyond the scope of this paper, but we have provided some considerations based on the traditionally defined α and how FORCAST observations to derive $\alpha(19\text{--}37\ \mu\text{m})$ may help. If the sources are indeed protostars, those same FORCAST observations can be used to estimate their internal luminosities by Equation (14), or Equation (16) specifically for 25.3 μm and 37.1 μm observations.

5.5. Envelope Mass

The assumptions and applicability of the Ulrich envelope density profile are important to consider, especially in the context of the high envelope masses relevant for protostar models. The assumptions include 1) free fall toward a central mass, $M_* + M_{\text{disk}}$, at the free-fall velocity given by

$$v_{\text{ff}} = \sqrt{\frac{2G(M_* + M_{\text{disk}})}{R_{\text{env}}}}; \quad (17)$$

setting $r = R_{\text{env}}$ to focus on effects near the adopted cloud boundary, and 2) pressure terms that are small compared to kinetic energy, which can be written as the condition

$$v_{\text{ff}} \geq a_s, \quad (18)$$

where a_s is the thermal sound speed of the gas. For example, the fiducial case of $R_{\text{env}} = 14,000\ \text{au}$ and $M_* + M_{\text{disk}} \approx M_* = 0.5 M_{\odot}$, as assumed in our modeling, results in $v_{\text{ff}} = 0.25\ \text{km s}^{-1}$, which is on the order of the thermal sound speed of $a_s = 0.19\ \text{km s}^{-1}$ for $T = 10\ \text{K}$ gas (e.g., Terebey et al. 1984). Thus, pressure terms are important near the adopted edge of the envelope, with the result that the density distributions in real protostellar envelopes will deviate from that given by the Ulrich profile near the envelope boundaries.

The first assumption, as expressed in Equation (17), applies if the central mass dominates the gravitational potential. However, the envelope masses considered here and in previous studies (e.g., Dunham et al. 2008), which also use the Ulrich envelope model, typically exceed the central masses. To evaluate the size of the effect, we compare the Ulrich envelope mass computed from Equation (7), which further assumes that the central mass is dominated by the star (i.e., $M_{\text{disk}} \ll M_*$), with that of the TSC84 (Terebey et al. 1984) self-consistent cloud collapse model. This comparison is appropriate because the TSC84 model includes pressure effects and asymptotically matches the Ulrich model at small radii.

In the TSC84 model, *outside* the collapsing region of the envelope *and* when rotational effects are small, a simple formula (involving the leading term) gives the total mass

interior to r (e.g., Equation (3) of TSC84; Shu 1977):

$$M_{\text{tot}} = \frac{2a_s^2 r}{G}, \quad (19)$$

where $r > R_{\text{exp}}(t)$, the radius of the expansion wave representing the boundary of the collapsing region at time t and given by $R_{\text{exp}}(t) = a_s t$. In terms of the mass infall rate, given by

$$\dot{M}_{\text{env}} = \frac{m_0 a_s^3}{G}, \quad (20)$$

where $m_0 = 0.975$ (Shu 1977), this total mass may be expressed as

$$M_{\text{tot}} = \left(\frac{2}{m_0} \right) \frac{\dot{M}_{\text{env}} r}{a_s}. \quad (21)$$

The difference between this total mass and the central mass, which has already collapsed to form the protostar and disk, is the desired envelope mass interior to $r > R_{\text{exp}}$ in the TSC84 model:

$$M_{\text{env}}^{\text{TSC84}} = M_{\text{tot}} - (M_* + M_{\text{disk}}). \quad (22)$$

Using Equation (21) to substitute for M_{tot} , and noting that the central mass is

$$M_* + M_{\text{disk}} = \dot{M}_{\text{env}} t, \quad (23)$$

the envelope mass interior to $r > R_{\text{exp}}$ is then given by

$$M_{\text{env}}^{\text{TSC84}} = \left(\frac{2}{m_0} - \frac{R_{\text{exp}}}{r} \right) \frac{\dot{M}_{\text{env}} r}{a_s}. \quad (24)$$

The factor in parenthesis has a value on the order of unity at $r = R_{\text{exp}}$ and on the order of 2 at $r \gg R_{\text{exp}}$. Thus, the factor in parenthesis ranges from about 1 to 2 over the valid $r \geq R_{\text{exp}}$ regime. Note that computing the envelope mass at smaller r requires using the full collapse solution, and can be done numerically, but it is not necessary for our purpose.

For direct comparison with the envelope mass in the Ulrich free-fall model, we rewrite Equation (7) in terms of v_{ff} , using Equation (17), to obtain

$$M_{\text{env}} = \left(\frac{2a_s}{3v_{\text{ff}}} \right) \frac{\dot{M}_{\text{env}} R_{\text{env}}}{a_s}, \quad (25)$$

which becomes the inequality

$$M_{\text{env}} \leq \frac{2}{3} \frac{\dot{M}_{\text{env}} R_{\text{env}}}{a_s}, \quad (26)$$

if indeed the pressure terms are small compared to kinetic energy (i.e., Equation (18)). This expression is similar in form to that of the TSC84 model in Equation (24) above and demonstrates that the Ulrich profile underestimates the envelope mass, compared with a realistic envelope model having both gravity and pressure terms. For the adopted case of $M_* = 0.5 M_{\odot}$, Figure 9 compares the envelope mass at different accretion rates and at fixed $r = R_{\text{env}} = 14,000\ \text{au}$ envelope radius. The mass difference is about a factor of two, large enough to be important at millimeter wavelengths where the observations are sensitive to cloud (i.e., envelope) mass. However, the mass difference is less important at the mid-infrared wavelengths relevant to this study, where the fluxes

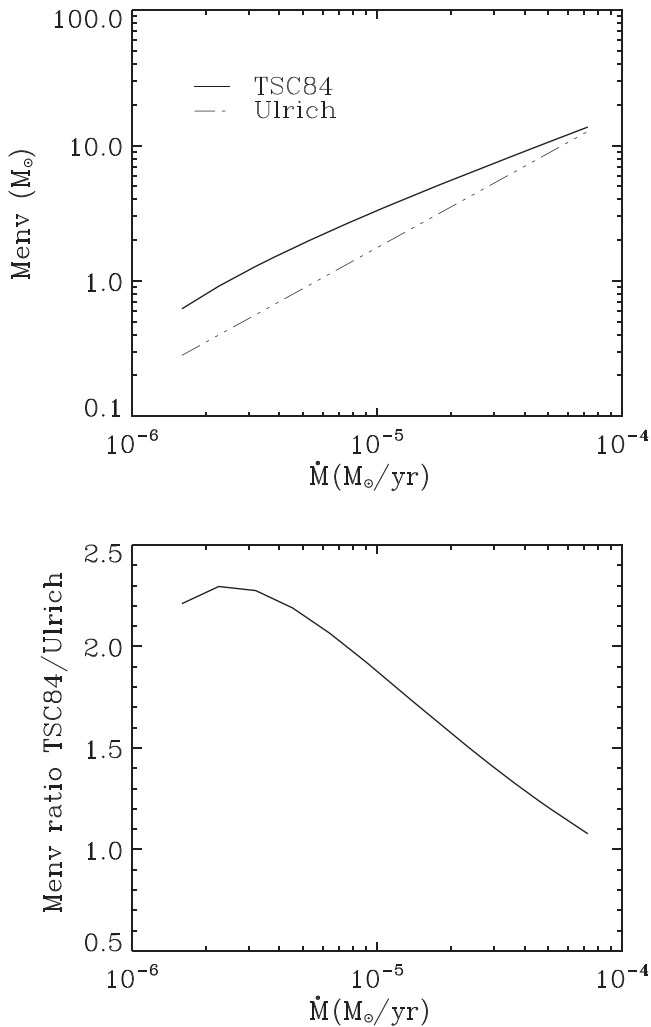


Figure 9. Comparison of M_{env} (top) and M_{env} ratio (bottom) between the TSC84 and Ulrich solutions as a function of mass infall rate, \dot{M}_{env} , for $M_* = 0.5 M_{\odot}$. The Ulrich solution underestimates the envelope mass for the protostar case.

generated are not sensitive to the treatment of the outer boundary (e.g., Whitney & Hartmann 1993).

6. Summary

In this study, we have established an approach whereby a pair of FORCAST filters may be used to estimate the luminosities of protostars. Empirical relationships are derived for different combinations of a long-wavelength filter (F 31.5 μm , F 33.6 μm , F 34.8 μm , and F 37.1 μm) paired with a short-wavelength filter (F 19.7 μm , F 24.2 μm , and F 25.3 μm). We find that the best pairing is F 37.1 μm with F 25.3 μm , resulting in luminosity estimates that are reliable to within a factor of 2.3 for 99% of protostars, which is comparable to the precision achievable in previous studies that used *Spitzer* or *Herschel* 70- μm data. The luminosity is estimated using Equation (16) once the flux densities $S_{\nu,37.1}$ and $S_{\nu,25.3}$ in Jy are known. Table 3 gives results for other FORCAST filter pairs, which may be used with Equations (14) and (15) to estimate luminosities.

With many protostars lacking data at wavelengths 70 μm or longer, obtaining FORCAST observations and applying our results may currently be the best approach to determine

their luminosities. Furthermore, the higher angular resolution achievable by FORCAST enables partitioning of emission among sources that were blended in previous observations and provides better constraints on the SEDs and luminosities of the components. Our approach requires data using only a pair of FORCAST filters, not a well-covered SED in the infrared and submillimeter regimes, and is independent of the inclination of the protostar.

In Section 2.1 we considered available dust model opacities. Figure 2 shows that the OH5 opacity (augmented with Pollack optical constants) fits the observational data best, although not perfectly. We find that an improved dust model would affect the luminosity estimates by only 5%–10%, thus supporting the choice of OH5 dust for protostellar envelopes.

We also compared (Section 5.5) the commonly assumed Ulrich density profile for protostellar envelopes with a more realistic profile for envelope masses comparable to, or greater than, the embedded source. Real protostellar envelopes likely have material that collapses more slowly than assumed free-fall velocities, and pressure terms become appreciable in the outer regions of the envelopes. These considerations suggest that the Ulrich profile underestimates total envelope masses by about a factor of two, but this deficiency has little effect on the observed infrared emission from the protostar.

We thank Joe Adams for providing FORCAST transmission curves for typical observing conditions, Michael Dunham for providing properties of OH5 dust, and Barbara Whitney for discussion of implementation of the external ISRF in HOCHUNK3D. S. Terebey thanks the Department of Astronomy at the University of Maryland for its hospitality. Simulations were performed on the YORP cluster administered by the Center for Theory and Computation, part of the Department of Astronomy at the University of Maryland. This study was based in part on observations made with the NASA/DLR Stratospheric Observatory for Infrared Astronomy (SOFIA). SOFIA is jointly operated by the Universities Space Research Association, Inc. (USRA), under NASA contract NAS2-97001, and the Deutsches SOFIA Institut (DSI) under DLR contract 50 OK 0901 to the University of Stuttgart. Financial support for this work was provided by NASA through awards SOF-0106 and SOF04-0173 issued through USRA.

Facility: SOFIA.

Software: HOCHUNK3D (Whitney et al. 2013), SOFIA Instrument Time Estimator (<https://dcs.sofia.usra.edu/proposal/Development/SITE/>).

ORCID iDs

Tracy L. Huard  <https://orcid.org/0000-0002-8187-6658>

References

- Adams, J. D., Herter, T. L., Gull, G. E., et al. 2010, *Proc. SPIE*, 7735, 77351U
- André, P., Men'shchikov, A., Bontemps, S., et al. 2010, *A&A*, 518, L102
- André, P., Ward-Thompson, D., & Barsony, M. 1993, *ApJ*, 406, 122
- Bjorkman, J. E. 1997, in *Stellar Atmospheres: Theory and Observations*, ed. J. P. De Greve, R. Blomme, & H. Hensberge (Berlin: Springer), 239
- Black, J. H. 1994, in *ASP Conf. Ser. 58, The First Symposium on the Infrared Cirrus and Diffuse Interstellar Clouds*, ed. R. M. Cutri & W. B. Latter (San Francisco, CA: ASP), 355
- Bolatto, A. D., Simon, J. D., Stanimirović, S., et al. 2007, *ApJ*, 655, 212
- Carlson, L. R., Sabbi, E., Sirianni, M., et al. 2007, *ApJL*, 665, L109
- Carlson, L. R., Sewilo, M., Meixner, M., et al. 2011, *ApJ*, 730, 78
- Carney, M. T., Yıldız, U. A., Mottram, J. C., et al. 2016, *A&A*, 586, A44

- Cassen, P., & Moosman, A. 1981, *Icar*, **48**, 353
- Chapman, N. L., Lai, S.-P., Mundy, L. G., et al. 2007, *ApJ*, **667**, 288
- Chapman, N. L., Mundy, L. G., Lai, S.-P., & Evans, N. J., II 2009, *ApJ*, **690**, 496
- Chiang, E. I., & Goldreich, P. 1997, *ApJ*, **490**, 368
- Crapsi, A., van Dishoeck, E. F., Hogerheijde, M. R., Pontoppidan, K. M., & Dullemond, C. P. 2008, *A&A*, **486**, 245
- Draine, B. T. 1978, *ApJS*, **36**, 595
- Dullemond, C. P., & Dominik, C. 2004, *A&A*, **417**, 159
- Dunham, M. M., Allen, L. E., Evans, N. J., II, et al. 2015, *ApJS*, **220**, 11
- Dunham, M. M., Crapsi, A., Evans, N. J., II, et al. 2008, *ApJS*, **179**, 249
- Dunham, M. M., Evans, N. J., II, Terebey, S., Dullemond, C. P., & Young, C. H. 2010, *ApJ*, **710**, 470
- Dunham, M. M., Stutz, A. M., Allen, L. E., et al. 2014, in *Protostars and Planets VI*, ed. H. Beuther et al. (Tucson, AZ: Univ. Arizona Press), 195
- Enoch, M. L., Evans, N. J., II, Sargent, A. I., & Glenn, J. 2009, *ApJ*, **692**, 973
- Evans, N. J., II, Allen, L. E., Blake, G. A., et al. 2003, *PASP*, **115**, 965
- Evans, N. J., II, Rawlings, J. M. C., Shirley, Y. L., & Mundy, L. G. 2001, *ApJ*, **557**, 193
- Fazio, G. G., Hora, J. L., Allen, L. E., et al. 2004, *ApJS*, **154**, 10
- Flaherty, K. M., Pipher, J. L., Megeath, S. T., et al. 2007, *ApJ*, **663**, 1069
- Forbrich, J., Tappe, A., Robitaille, T., et al. 2010, *ApJ*, **716**, 1453
- Furlan, E., Fischer, W. J., Ali, B., et al. 2016, *ApJS*, **224**, 5
- Gramajo, L. V., Whitney, B. A., Gómez, M., & Robitaille, T. P. 2010, *AJ*, **139**, 2504
- Greene, T. P., Wilking, B. A., Andre, P., Young, E. T., & Lada, C. J. 1994, *ApJ*, **434**, 614
- Haisch, K. E., Jr., Barsony, M., Ressler, M. E., & Greene, T. P. 2006, *AJ*, **132**, 2675
- Hartmann, L. 1998, *Accretion Processes in Star Formation* (Cambridge: Cambridge Univ. Press)
- Harvey, P., Merín, B., Huard, T. L., et al. 2007, *ApJ*, **663**, 1149
- Harvey, P. M., Fallscheer, C., Ginsburg, A., et al. 2013, *ApJ*, **764**, 133
- Hatchell, J., Fuller, G. A., Richer, J. S., Harries, T. J., & Ladd, E. F. 2007, *A&A*, **468**, 1009
- Herter, T. L., Adams, J. D., De Buizer, J. M., et al. 2012, *ApJL*, **749**, L18
- Horn, J. M. M., & Becklin, E. E. 2001, *PASP*, **113**, 997
- Indebetouw, R., Mathis, J. S., Babler, B. L., et al. 2005, *ApJ*, **619**, 931
- Kim, S.-H., Martin, P. G., & Hendry, P. D. 1994, *ApJ*, **422**, 164
- Kryukova, E., Megeath, S. T., Gutermuth, R. A., et al. 2012, *AJ*, **144**, 31
- Lada, C. J. 1987, in *IAU Symp. 115, In Star-forming Regions*, ed. M. Peimbert & J. Jugaku (Cambridge: Cambridge Univ. Press), 1
- Lazareff, B., Monin, J.-L., & Pudritz, R. E. 1990, *ApJ*, **358**, 170
- Mathis, J. S., Mezger, P. G., & Panagia, N. 1983, *A&A*, **128**, 212
- Maury, A. J., André, P., Men'shchikov, A., Könyves, V., & Bontemps, S. 2011, *A&A*, **535**, A77
- Megeath, S. T., Gutermuth, R., Muzerolle, J., et al. 2012, *AJ*, **144**, 192
- Merín, B., Jørgensen, J., Spezzi, L., et al. 2008, *ApJS*, **177**, 551
- Ormel, C. W., Min, M., Tielens, A. G. G. M., Dominik, C., & Paszun, D. 2011, *A&A*, **532**, A43
- Ossenkopf, V., & Henning, T. 1994, *A&A*, **291**, 943
- Pollack, J. B., Hollenbach, D., Beckwith, S., et al. 1994, *ApJ*, **421**, 615
- Poulton, C. J., Robitaille, T. P., Greaves, J. S., et al. 2008, *MNRAS*, **384**, 1249
- Pringle, J. E. 1981, *ARA&A*, **19**, 137
- Rebull, L. M., Padgett, D. L., McCabe, C.-E., et al. 2010, *ApJS*, **186**, 259
- Rieke, G. H., Young, E. T., Engelbracht, C. W., et al. 2004, *ApJS*, **154**, 25
- Sadavoy, S. I., Di Francesco, J., André, P., et al. 2014, *ApJL*, **787**, L18
- Samal, M. R., Pandey, A. K., Ojha, D. K., et al. 2012, *ApJ*, **755**, 20
- Seale, J. P., & Looney, L. W. 2008, *ApJ*, **675**, 427
- Shakura, N. I., & Sunyaev, R. A. 1973, *A&A*, **24**, 337
- Shirley, Y. L., Huard, T. L., Pontoppidan, K. M., et al. 2011, *ApJ*, **728**, 143
- Shirley, Y. L., Nordhaus, M. K., Grevech, J. M., et al. 2005, *ApJ*, **632**, 982
- Shu, F. H. 1977, *ApJ*, **214**, 488
- Simon, J. D., Bolatto, A. D., Whitney, B. A., et al. 2007, *ApJ*, **669**, 327
- Stutz, A. M., Tobin, J. J., Stanke, T., et al. 2013, *ApJ*, **767**, 36
- Suutarinen, A., Haikala, L. K., Harju, J., et al. 2013, *A&A*, **555**, A140
- Terebey, S., Fich, M., Noriega-Crespo, A., et al. 2009, *ApJ*, **696**, 1918
- Terebey, S., Shu, F. H., & Cassen, P. 1984, *ApJ*, **286**, 529
- Tobin, J. J., Looney, L. W., Mundy, L. G., Kwon, W., & Hamidouche, M. 2007, *ApJ*, **659**, 1404
- Ulrich, R. K. 1976, *ApJ*, **210**, 377
- Whitney, B. A., & Hartmann, L. 1993, *ApJ*, **402**, 605
- Whitney, B. A., Indebetouw, R., Bjorkman, J. E., & Wood, K. 2004, *ApJ*, **617**, 1177
- Whitney, B. A., Robitaille, T. P., Bjorkman, J. E., et al. 2013, *ApJS*, **207**, 30
- Whitney, B. A., Sewilo, M., Indebetouw, R., et al. 2008, *AJ*, **136**, 18
- Whitney, B. A., Wood, K., Bjorkman, J. E., & Cohen, M. 2003a, *ApJ*, **598**, 1079
- Whitney, B. A., Wood, K., Bjorkman, J. E., & Wolff, M. J. 2003b, *ApJ*, **591**, 1049
- Wood, K., Bjorkman, J. E., Whitney, B. A., & Code, A. D. 1996, *ApJ*, **461**, 828
- Wood, K., Wolff, M. J., Bjorkman, J. E., & Whitney, B. 2002, *ApJ*, **564**, 887
- Yorke, H. W., & Bodenheimer, P. 1999, *ApJ*, **525**, 330
- Young, E. T., Becklin, E. E., Marcum, P. M., et al. 2012, *ApJL*, **749**, L17
- Young, K. E., Harvey, P. M., Brooke, T. Y., et al. 2005, *ApJ*, **628**, 283
- Zhang, Y., Tan, J. C., & McKee, C. F. 2013, *ApJ*, **766**, 86